

1 **Time-lapse monitoring of root water uptake using electrical resistivity** 2 **tomography and Mise-à-la-Masse: a vineyard infiltration experiment**

3 Benjamin Mary¹, Luca Peruzzo^{2,3}, Jacopo Boaga¹, Nicola Cenni¹, Myriam Schmutz³, Yuxin Wu², Susan
4 S. Hubbard², Giorgio Cassiani¹

5 ¹Dipartimento di Geoscienze, Università degli Studi di Padova, Via G. Gradenigo, 6–35131 Padova, Italy

6 ²Earth and Environmental Sciences Area, Lawrence Berkeley National Laboratory, 1 Cyclotron Rd, Berkeley, CA, 94720,
7 USA.

8 ³EA G&E 4592, Bordeaux INP, University Bordeaux Montaigne, 1 allée Daguin, 33607 Pessac, France

9 Correspondence to: Benjamin Mary (benjamin.mary@unipd.it)

10 **Abstract.** This paper presents a time-lapse application of electrical methods (Electrical Resistivity Tomography – ERT – and
11 Mise-à-la-Masse – MALM) for monitoring plant roots and their activity (root water uptake) during a controlled infiltration
12 experiment. The use of non-invasive geophysical monitoring is of increasing interest as these techniques provide time-lapse
13 imaging of processes that otherwise can only be measured at few specific spatial locations. The experiment here described was
14 conducted in a vineyard in Bordeaux (France) and was focused on the behaviour of two neighbouring grapevines. The joint
15 application of ERT and MALM has several advantages. While ERT in time-lapse mode is sensitive to changes in soil electrical
16 resistivity and thus to the factors controlling it (mainly soil water content, in this context), MALM uses DC current injected in
17 a tree stem to image where the plant-root system is in effective electrical contact with the soil at locations that are likely to be
18 the same where root water uptake (RWU) takes place. Thus, ERT and MALM provide complementary information about the
19 root structure and activity. The experiment shows that the region of likely electrical current sources produced by MALM does
20 not change significantly during the infiltration time in spite of the strong changes of electrical resistivity caused by changes in
21 soil water content. Ultimately, the interpretation of the current source distribution strengthened the hypothesis of using current
22 as a proxy for root detection. This fact, together with the evidence that current injection in the soil and in the stem produce
23 totally different voltage patterns, corroborates the idea that this application of MALM highlights the active root density in the
24 soil. When considering the electrical resistivity changes (as measured by ERT) inside the stationary volume of active roots
25 delineated by MALM, the overall tendency is towards a resistivity increase during irrigation time, which can be linked to a
26 decrease in soil water content caused by root water uptake. On the contrary, when considering the soil volume outside the
27 MALM-derived root water uptake region, the electrical resistivity tends to decrease as an effect of soil water content increase
28 caused by the infiltration. The use of a simplified infiltration model confirms at least qualitatively this behaviour. The
29 monitoring results are particularly promising, and the method can be applied to a variety of scales including the laboratory
30 scale where direct evidence of roots structure and root water uptake can help corroborate the approach. Once fully validated,
31 the joint use of MALM and ERT can be used as a valuable tool to study the activity of roots under a wide variety of field
32 conditions.

33

34 **1 Introduction**

35 The interaction between soil and biota is one of the main mechanisms controlling the exchange of mass and energy between
36 the Earth's terrestrial ecosystems and the atmosphere. Philip (1966) was the first to use the phrase “soil–plant–atmosphere
37 continuum” (SPAC) to conceptualize this interface in the framework of continuum physics. Even though more than five
38 decades have elapsed and many efforts have been expanded (e.g., Maxwell et al., 2007; de Arellano et al., 2012; Anderegg et
39 al., 2013; Band et al., 2014), the current mechanistic understanding or modelling of SPAC is still unsatisfactory (e.g. Dirmeyer
40 et al., 2006, 2014 and Newman et al., 2006). This is not totally surprising, since soil-plant interactions are complex, exhibiting
41 scale- and species-dependence with high soil heterogeneity and plant growth plasticity. In this study, we focus on new methods

42 designed to image root systems and their macroscopic functioning, in order to help understand the complex mechanisms of
43 these systems (the rhizosphere, e.g. York et al., 2016). This diversity of interactions presents an enormous scientific challenge
44 to understanding the linkages and chain of impacts (Richter and Mobley, 2009).

45 Roots contribute substantially to carbon sequestration. Roots are the connection between the soil, where water and nutrients
46 reside, to the other organs and tissues of the plant, where these resources are used. Hence roots provide a link in the pathway
47 for fluxes of soil water and other substances through the plant canopy to the atmosphere (e.g. Dawson and Stiegwolf, 2007).
48 These transpiration fluxes are responsible for the largest fraction of water leaving the soil in vegetated systems (Chahine,
49 1992). Root Water uptake (RWU) influences the water dynamics in the rhizosphere (Couvreur et al., 2012) and the partitioning
50 of net radiation into latent and sensible heat fluxes thereby impacting atmospheric boundary layer dynamics (Maxwell et al.,
51 2007; de Arellano et al., 2012). Yet, a number of issues remain when representing RWU in both hydrological and atmospheric
52 models. Dupuy et al. (2010) summarize the development of root growth models from its origins in the 1970s with simple
53 spatial models (Hackett and Rose, 1972; Gerwitz and Page, 1974) to the development of very complex plant architectural
54 models (Jourdan and Rey, 1997). Dupuy et al. (2010) advocate for a different approach, where roots systems are described as
55 “density” distributions. Attempts in this direction (Dupuy et al., 2005; Draye et al., 2010; Dupuy and Vignes, 2012) require
56 much less specific knowledge of the detailed mechanisms of meristem evolution, and yet are sufficient to describe the root
57 “functions” in the framework of continuum physics, i.e. the one endorsed by the SPAC concept. These models also lend
58 themselves more naturally to calibration against field evidence, as they focus on the “functioning” of roots, especially in terms
59 of RWU (e.g. Volpe et al., 2013, Manoli et al., 2014). However, calibration requires that suitable data such as root density and
60 soil water content evolution are available in a form comparable with the model to be calibrated. This is the main motivation
61 behind the work presented herein.

62 A thorough understanding of root configuration in space and their evolution in time is impossible to achieve using only
63 traditional invasive methods: this is particularly true for root hairs, i.e. for the absorptive unicellular extensions of epidermal
64 cells of a root. These tiny, hair-like structures function as the major site of water and mineral uptake. Root hairs are extremely
65 delicate, turn over quickly, and are subject to desiccation and easily destroyed. For these reasons, direct investigation of their
66 in situ structure via excavation is practically impossible under field conditions.

67 The development of non-invasive or minimally invasive techniques is required to overcome the limitations of conventional
68 invasive characterization approaches. Non-invasive methods are based on physical measurements at the boundary of the
69 domain of interest, i.e. at the ground surface and, when possible, in shallow boreholes. Non-invasive methods provide spatially
70 extensive, high-resolution information that can also be supported by more traditional local and more invasive data such as soil
71 samples, TDR, lysimeters and rhizotron measurements.

72 Electrical signals may contribute to the detection of roots and to the characterization of their activities. For instance, self-
73 potential (SP) signals can be associated with plant activities: water uptake generates a water circulation and a mineral
74 segregation at the soil–roots interface that induce ionic concentration gradients which in turn generate voltages of the order of
75 a few mV (Gibert et al., 2006). However, such SP sources are generally too low to be detectable in normally noisy environment.
76 Induced Polarization (e.g. Kemna et al., 2012) is also a promising approach in root monitoring. This is consistent with the fact
77 that root systems are commonly modelled as electrical circuits composed of resistance R and capacitance C (e.g. Dalton, 1995
78 and similar models). Recently, Mary et al. (2017) considered polarization from soil to root tissues, as well as the polarization
79 processes along and around roots, to explain the phase shift (between injected current and voltage response) observed for
80 different soil water content. Weigand and Kemna (2017, 2019) demonstrated that multi-frequency electrical impedance
81 tomography is capable of imaging root systems extent.

82 In the investigation of roots and RWU the most widely used non-invasive technique is Electrical Resistivity Tomography (ERT
83 – e.g. Binley and Kemna, 2005). ERT measures soil electrical resistivity and, in time-lapse mode, resistivity changes over
84 time. Electrical resistivity values depend on soil type and its porosity, but also on state variables such as the saturation of

85 electrolyte (water) in the pores, and the concentration of solutes in the pore water (as described e.g. by the classical Archie's
86 law, 1942). Note, however, that other factors may play a role, such as clay content (Rhoades et al., 1976; Waxman and Smits,
87 1968) and temperature (e.g., Campbell et al., 1949). However, in general, it is possible to estimate water content changes from
88 changes in electrical resistivity over time (and space) provided that pore water salinity does not vary dramatically. While ERT
89 has been attempted for quantifying root biomass on herbaceous plants (e.g. Amato et al., 2009), the main use of this technique
90 in this context aims at identifying changes in soil water content in space and evolution in time (e.g., Michot et al., 2003, 2016;
91 Srayeddin and Doussan, 2009; Garré et al., 2011; Cassiani et al., 2012, Brillante et al. 2015). With specific reference to RWU,
92 Cassiani et al. (2015, 2016), Consoli et al. (2017) and Vanella et al. (2018) used time-lapse ERT with 3D cross-hole
93 configurations to monitor changes in soil electrical resistivity caused by irrigation and RWU for different crops (apple and
94 citrus trees). It should also be noted that RWU and the release of different exudates by fine roots modify soil water content and
95 resistivity at several temporal scales (York et al., 2016).

96 On the other hand, evidence suggests that roots themselves may produce signals in ERT surveys (Amato et al., 2008; Werban
97 et al., 2008); however, these signals are often difficult to separate from soil heterogeneities and soil water content variations
98 in space (Rao et al., 2019). Nevertheless, in most cases, the ranges of electrical resistivity of soil and roots overlap, and while
99 the amplitude of contrasts varies according to the soil resistivity and tree species (e.g. Mary et al., 2016), the direct
100 identification of root systems using ERT is often impractical.

101 Recently, the Mise-A-La-Masse (MALM) method has been proposed for plant root mapping. MALM is a classical electrical
102 method (Parasnis, 1967) originally developed for mining exploration, but also used more recently e.g. in the context of landfill
103 characterization (De Carlo et al., 2013) as well as conductive tracer test monitoring (Osiensky, 1997; Perri et al., 2018). In
104 MALM, an electrical current is injected into a conductive body with a return current electrode far away ("at infinity"), and the
105 resulting voltage is measured at the ground surface or in boreholes, again with a reference electrode at infinity: the shape of
106 voltage contour lines is informative about the extent and orientation of the conductive body. This idea can be applied to the
107 plant stem and roots system, considering that electrical current can be transmitted through the xylem and phloem (on either
108 side of the cambium), where sap flow takes place. The main assumption is that fine root connections and mycorrhiza at the
109 contact between roots and soil convey the injected current into the soil where this contact is efficient, thus appearing as a
110 distribution of current sources in the ground. The location of these sources should correspond to the locations of active contacts
111 between roots and soil, and could be identified starting from the measured voltage distribution at the ground surface or in
112 boreholes. This approach has been recently tested by Mary et al. (2018, 2019) on vine trees and citrus trees, showing that
113 current injection in the stem and in the soil just next to the stem produces very different voltage patterns, thus confirming that
114 the stem-roots system conveys current differently from a direct injection in the ground.

115 In this study we present the results of an infiltration experiment conducted in a Bordeaux vineyard (France). This paper is
116 meant to be an extension of Mary et al. (2018) and to focus on the results of an infiltration experiment. The experiment was
117 monitored (also) using time-lapse 3D ERT and time-lapse MALM measurements, the latter performed by injecting current in
118 the vine trees stems. This study had the following goals:

- 119 (a) define a non-invasive investigation protocol capable of "imaging" the root activity as well as the distribution of active
120 roots, at least in terms of their continuum description mentioned above, under varying soil water content conditions;
- 121 (b) integrate the geophysical results with mass fluxes measurements in/out of the soil-plant continuum system using a
122 simple 1D simulation reproducing the infiltration experiment.
- 123 (c) give recommendations for future experiments focusing on the method validation.

124

125 **2 Methodology**

126 **2.1 Site description**

127 The study was conducted in a commercial vineyard (Chateau La Louviere, Bordeaux) in the Pessac Leognan Appellation of
128 France (long 44°44'15''N, lat 0°34'45''W). The climate of the region is oceanic with a mean annual air temperature of 13.7
129 °C and about 800 mm annual precipitation. Grapevine trees are planted at 1 m distance along the rows, and the rows are spaced
130 about 1.5 m. We focused our interest on two neighbouring plants.

131 The vineyard is not irrigated. The soil is sandy down to 1 m depth with sandy clay below, down to 1.75 m, and calcareous at
132 depth. Due to its larger particles and thus smaller surface area, the sandy layer has a relatively poor water retention capacity.
133 Nevertheless, the water supply of the vine plant is not a limiting factor (refer to Fig. 2 and Mary et al. (2018) for more details
134 about the plants and soil type). We concentrated our monitoring on only two neighbouring grapevines (Fig. 1), which differ in
135 age and size: plant A was smaller and younger, plant B was considerably larger and older.

136 **2.2 Meteorological measurements and irrigation schedule**

137 Hourly meteorological data were acquired by an automatic weather station located about 300 m from the plot and managed by
138 DEMETER (Agrometeorological Service - www.meteo-agriculture.eu/qui-sommes-nous/lhistoire-de-demeter). These
139 micrometeorological data were valuable to estimate the initial soil conditions and the changes in time (Figure 2). Potential
140 evapotranspiration (ETP) was computed according to the Penman-Monteith formula accounting for the incoming short-wave
141 solar radiation, air temperature, air humidity, wind speed and rainfall measured by the station. Prior to June 19, 2017, date of
142 the first field data acquisition, little precipitation was recorded for 5 days (only 2.5mm on June 13) and only 18mm cumulative
143 precipitation was recorded during the entire month of June 2017. The mean air temperature was very high (35°C under a well-
144 ventilated shelter). Consequently, the plants were probably suffering from water deficit at the time of the experiment. Thus, at
145 the start of the experiment, we assumed that the soil water content (SWC) around the plants was probably below to field
146 capacity. As shown in Figure 2, the evapotranspiration rate was about 5.6 mm/day.

147 The controlled infiltration experiment was conducted using a sprinkler installed between the two monitored plants, placed at
148 an elevation of 1.4m, in order to apply irrigation water as uniformly as possible. The irrigation started on June 19, 2017 at
149 13h00 and ended two hours later (15h00) for a total of 260 litres (104 l/h). Runoff was observed due to topography and probably
150 induced more water supply for plant A that is located downhill. The irrigation water had an electrical conductivity of 720µS/cm
151 at 15°C.

152 **2.3 ERT and MALM data acquisition**

153 We carried out a time-lapse ERT acquisition, based on custom-made ERT boreholes (six of them, each with 12 electrodes),
154 plus surface electrodes (Fig. A1). The six boreholes were placed to form two equal rectangles at the ground surface. Each
155 rectangle size was 1 m by 1.2m respectively in the row and inter-row line directions, with a vine tree placed at the centre of
156 each rectangle. The boreholes were installed in June 2015 and a good electrical contact with soil was already achieved at the
157 time of installation. The topmost electrode in each hole was 0.1 m below ground, with vertical electrode spacing along each
158 borehole equal to 0.1 m. In each rectangle, 24 surface stainless steel electrodes (14mm diameter), spaced 20 cm in both
159 horizontal directions, surrounded the plant stem arranged in a five by five regular mesh (with one skipped electrode near the
160 stem). Note that after testing smaller electrode size in surface, we finally adopted larger ones since they ensured a better contact
161 in the loose soil and were heavier and more firmly grounded (3cm out of 12) to resist irrigation. We conducted the acquisitions
162 on each rectangle independently. Each acquisition was therefore performed using 72 electrodes (24 surface and 48 electrodes
163 in 4 boreholes) using an IRIS Syscal Pro resistivity meter. For all measurements we used a skip 2 dipole-dipole acquisition

164 (i.e., a configuration where the current dipoles and potential dipoles are three times larger than the minimal electrode spacing).
165 The total dataset includes three types of measurements: 430 surface-to-surface, 2654 surface-to-borehole and 4026 in-hole
166 measurements.
167 In addition to acquiring ERT data, we also acquired MALM data. MALM acquisition was logistically the same as ERT and
168 was supported by the same device, but used a pole-pole scheme (with two remote electrodes). Borehole and surface electrodes
169 composing the measurement setup were used as potential electrodes, while current electrode C1 was planted directly into the
170 stem, 10 cm from the soil surface, with an insertion depth of about 2 cm, in order to inject current directly into the cambium
171 layer. The two remote electrodes C2 (for current) and P2 (for voltage) were placed approximatively at 30m distance from the
172 plot, in opposite directions. Note that for MALM (unlike than for ERT), one corner surface electrode was put near the stem in
173 order to refine the information at the centre of each rectangle.
174 Each MALM acquisition was accompanied by a companion MALM acquisition where the current electrode C1 was placed
175 directly in the soil next to the stem rather than in the stem itself. In this way the effect of the plant stem-root system in conveying
176 current can be evidenced directly comparing the resulting voltage patterns resulting from the two MALM configurations.
177 For both ERT and MALM, we acquired both direct and reciprocal configurations (that swap current and voltage electrode
178 pairs), in order to assess the reciprocal error as an estimate of measurement error (see e.g. Cassiani et al., 2006). Note that for
179 the MALM case, reciprocals may not be the best solutions to estimate data quality as it has been shown in Mary et al. (2018),
180 possibly because of non-linearity caused by current injection in the stem.
181 We adopted a time-lapse approach, conducting repeated ERT and MALM acquisitions over time in order to assess the evolution
182 of the system's dynamics under changing moisture conditions associated with the infiltration experiment. We conducted
183 repeated measurements starting on 19 June 2017 at 10:20 LT, and ending the next day at about 17:00 LT. The schedule of the
184 acquisitions and the irrigation times is reported in Table 1.

185 **2.4 Forward hydrological model and comparison with geophysical results**

186 Hydrus 1D (Simunek, J. et al., 1998) was used to simulate cumulative infiltration and water content distributions for plant B
187 (the larger one). The results from geophysical data acquisition were used to feed the hydrological model initial conditions.
188 Boundary conditions were set for the column respectively as an atmospheric BC with surface run off (observed during the
189 experiment) and triggered irrigation for the upper part, and free drainage for the lower part (see Figure 2). We assumed that
190 the retention and hydraulic conductivity functions can be represented by the Mualem-van Genuchten model (MVG, Mualem,
191 1976; van Genuchten, 1980). Soil hydraulic parameters were directly inferred using grain size distribution and the pedo-
192 transfer functions from the Rosetta software (Schaap et al., 2001). From the pit information (Mary et al., 2018), we assumed a
193 uniform soil type along a 1D column ranging from 0 to 1.2m depth (Figure 2c). We used two types of time variable boundary
194 conditions: (i) the irrigation rate changing with time, which was measured during the course of the experiment, and (ii) the
195 potential evapotranspiration estimated according to meteorological data. We neglected direct evaporation. The root profile has
196 been inferred from the MALM result at background (pre-irrigation) time using the average value along horizontal planes
197 (Figure 2b) discretised every 20cm. We used the functional form of RWU proposed by Feddes et al. (1978) with no water
198 stress compensation and a non-uniform root profile between 0 and 0.7 m depth.
199 The link between the forward hydrological and the geophysical model is a petrophysical relation which transforms electrical
200 resistivity distributions into the corresponding simulated water content (θ_{ERT}) distributions. There are several petrophysical
201 models of varying complexity to relate water content with electrical resistivity (e.g. Archie, 1942; Waxman and Smits, 1968;
202 Rhoades et al., 1976; Mualem and Friedman, 1991). We adopted Archie's approach with the following parameters: pore water
203 conductivity was assumed equal to the electrical conductivity of the water used for the irrigation (720 $\mu\text{S}/\text{cm}$) for all the time
204 steps. The porosity was assumed to be equal to the soil saturated water content (θ_s), the cementation factor (m) equal to 1.3

205 and the saturation exponent (n) equal to 1 (typical values notably described in Werban et al., 2008). We considered
 206 homogenous soil distribution, so only one petrophysical relationship was necessary. Initial water content was inferred after
 207 transformation and reduction by averaging to 1D the ER values obtained during background time T_0 . We obtained a non-
 208 homogeneous initial water content for the hydrological simulation varying from 0.1 to 0.27 cm³.cm⁻³ (Fig. 2a). In order to
 209 compare the model results with the geophysical data, we used control points at 0, 0.2, 0.4, 0.6, 0.8m depth.

210 **2.5 Data analysis and processing**

211 **2.5.1 Micro-ERT time lapse analysis**

212 The inversion of ERT data was conducted using the classical Occam's approach (Binley and Kemna, 2005). We conducted
 213 both absolute inversions and time-lapse resistivity inversions, as done in other papers (e.g. Cassiani et al., 2015, 2016). We
 214 used for inversion only the data that pass the 10% reciprocal error criterion at all measurement times. A large percentage of
 215 the data had reciprocity errors below this threshold. We inverted the data using the R3t code (Binley, 2019) adopting a 3-D
 216 mesh with very fine discretization between the boreholes, while larger elements were used for the outer zone. Most of the
 217 inversions converged after fewer than 5 iterations, and the final RMS errors respect the set convergence criteria (Table 1). For
 218 the time lapse inversion, we followed the procedure described e.g. in Cassiani et al. (2006) in order to get rid of systematic
 219 errors and highlight changes in term of percentage of ER ratios compare to the background time. Time-lapse inversions were
 220 run at a lower error level (consistently with the literature – e.g. Cassiani et al., 2006) equal to 5%. At this threshold 65% (in
 221 mean) of the data passed the reciprocity. A total number of 687 points were used during the inversion after selection of common
 222 set between all-time steps.

223 **2.5.2 MALM modelling and source inversion**

224 The MALM processing applied to a plant is thoroughly described in Mary et al (2018). Here we only recall the mathematical
 225 background on which the method relies on and some advances compare to the previous approach described by Mary et al.
 226 (2018).

227 In MALM, we measure the voltage V (with respect to the remote electrode) at N points, corresponding to the N electrodes
 228 locations, x_1, x_2, \dots, x_N . Voltage depends on the density of current sources C according to Poisson's equation:

$$229 \quad \nabla \cdot (\sigma \nabla V) = C \quad , \quad (1)$$

230 where σ is the conductivity of the medium, here assumed to be defined by the conductivity distribution obtained from ERT
 231 data inversion. The main idea behind the source inversion is to identify the distribution of M current sources $C(x,y,z)$ – in
 232 practice located at the mesh nodes $C=[C_1, C_2, \dots, C_M]$ – that produce the measured voltage V distribution in space. Given a
 233 distribution of current sources, and once $\sigma(x,y,z)$ is known from ERT inversion, the forward problem is uniquely defined and
 234 consists in the calculation of the resulting V field. Conversely, the identification of $C(x,y,z)$ distribution given $V(x,y,z)$ and
 235 $\sigma(x,y,z)$ is an ill-posed problem, that requires regularization and/or a priori assumptions in order to deliver stable results.
 236 Different approaches are possible – for a detailed analysis in this context see Mary et al. (2018). In this paper we have used
 237 the simplest approach, i.e. we assumed that one single current source was responsible for the entire voltage distribution. For
 238 each candidate location the sum of squares between computed and measured voltages was used as an index of misfit of that
 239 location as a possible MALM current source in the ground. Mary et al. (2018) introduced a simple index that can be mapped
 240 in the three-dimensional soil space and that measures the misfit that a specific location is the (single) current source generating
 241 the observed voltage field. This index (F_I) is defined as:

$$242 \quad F_{1,i}(\mathbf{d}_m, \mathbf{d}_{f,i}) = \|\mathbf{d}_m - \mathbf{d}_{f,i}\|_2^2 \quad , \quad (2)$$

243 where \mathbf{d}_m is a vector of measured voltage (normalised), and $\mathbf{d}_{f,i}$ is a vector of modelled voltage corresponding to a single
 244 source injecting the entire known injected current at the i -th node in the mesh. The forward modelling producing the $\mathbf{d}_{f,i}$ values

245 is based on the direct solution of the DC current flow in a heterogeneous medium, such as implement in the R3t Finite Element
246 code (Binley, 2019). Thus, the F_1 inversion accounts naturally for the heterogeneous electrical resistivity of the 3D soil volume,
247 also in its evolution over time (e.g. as an effect of irrigation and RWU).

248 A more advanced objective function, which considers the presence of distributed sources, has also been introduced by Mary
249 et al. (2018). Here we propose several important changes to that approach, on the basis of the work by Peruzzo et al. 2019 who
250 proposed a linearized form of the problem. In this case, the cost function F_2 consists of error-weighted data misfit Φ_d and
251 model roughness Φ_m containing model relative smallness and smoothness both weighted by the regularization parameter λ :

$$252 \quad F_2 = \Phi_d(\mathbf{m}) + \lambda\Phi_m(\mathbf{m}) = \|\mathbf{W}_\varepsilon(\mathbf{d}_m - \mathbf{f}(\mathbf{m}))\|_2^2 + \lambda(\|\mathbf{W}_s(\mathbf{m} - \mathbf{m}_0)\|_2^2) . \quad (3)$$

253

254 Given a set of N voltage measurements, minimization of the objective function, F_2 , given by Eq. (3), produces a vector of M
255 current sources densities \mathbf{c}_j ($j = 1, 2, \dots, M$), where \mathbf{d}_m is the data vector, $\mathbf{f}(\mathbf{m})$ is the forward model that relates the model \mathbf{m} to
256 the resistances, \mathbf{W}_s is a smoothness operator, \mathbf{W}_ε is an error weighting matrix, and λ is a regularization parameter that
257 determines the amount of smoothing imposed on m during the inversion. An L-curve analysis is used to identify the optimal
258 regularisation parameter λ . In the revised algorithm all candidate current sources are kept during the inversion. Thus, there is
259 no more a need to identify a threshold for which some sources are rejected. However, the misfit of F_1 is transformed into a
260 normalized initial model (\mathbf{m}_0) of current density via the inverse ($1/F_1$) transformation. During the inversion of the current
261 density, we adopted a relative smallness regularisation as a prior criterion for the inversion i.e. the algorithm minimizes $\|\mathbf{m} -$
262 $\mathbf{m}_0\|^2$, where \mathbf{m}_0 is a reference model to which we believe the physical property distribution should be close. Lastly, current
263 conservation was respected since the sum of \mathbf{c}_j was equal to 1 at the end of the inversion iterations.

264 **3 Results**

265 **3.1 Background, irrigation time and monitoring of ERT measured data**

266 The soil electrical conductivity during the period prior to irrigation (see ERT results in Figure 2a and 3b, respectively for plants
267 A and B) ranged from 50 to 200 Ωm , with a median value around 100 Ωm , a range that is reasonable for a dry sandy soil. For
268 plant A, the smaller plant, the highest resistivity values were distributed at about 0.5 m depth (Figure 2a). For the larger plant
269 B (Figure 2), the positive resistivity anomalies are more diffused and less resistive (150 Ωm) compared to plant A, which
270 reach larger depths. The very small-scale anomalies observed at the soil surface are likely to be caused by heterogeneous direct
271 evaporation patterns or different soil compaction. The background time (T_0) for both plants revealed a low resistive layer
272 ranging in depth from 0 to 0.35 m for plant A and from 0 to 0.25 m for plant B. More interesting are the resistive anomalies at
273 intermediate depths. As observed in other case studies (e.g. Cassiani et al., 2015, 2016, Consoli et al., 2017; Vanella et al.
274 2018), these higher resistivity values are likely to be linked to soil saturation decrease caused by RWU, particularly in
275 consideration of its intensity during this time of the year (June) for non-irrigated crops. Of course, we cannot fully exclude that
276 higher resistivity is also related to woody roots presence, especially when they are dense. Besides, roots could also have
277 induced soil swelling creating voids acting like resistive heterogeneities.

278 The T_1 time step was collected during the irrigation, at 2h for plant A and at 30 minutes for plant B after the beginning of the
279 irrigation, so the variations of ER values are not directly comparable for the two plants. Figure 4a shows the resistivity
280 distribution during irrigation (at time step T_1) and after irrigation (T_2 to T_5) for plant B. The input of low resistivity water
281 (13.88 Ωm , measured in laboratory) caused a homogeneous drop of the resistivity values (as much as 100 Ωm difference)
282 around plant B. The observed resistivity decrease in the upper 40 cm can be attributed to the presence of a porous layer, and
283 correspondingly fast infiltration. A similar drop can be seen for the plant A (Fig. B1). This is an indirect evidence that water
284 infiltrated in both areas (that are next to each other) with no difference in soil hydraulic properties. For the time after irrigation,

285 it is difficult to appreciate the change in resistivity from the absolute values while time-lapse inversion (Fig. 4b) shows that
 286 the main increase in ER (up to 140% of the background value), was located in the upper layers (< 0.3m depth) and occurred
 287 between the background time and T₃. Note that the acquisition time T₃ corresponds to the morning of the following day, since
 288 no measurement were taken overnight, and the acquisition time match with the start of the increase of ET and mean air
 289 temperature. No increase was observed on plant A (Fig. B1). After T₃, no positive change in ER was observed.

290 3.2 Background and irrigation time steps of MALM measured data

291 Figure 5 shows the raw results of MALM acquisition on plant B, during background and irrigation, for both soil and stem
 292 injection configurations. Note that voltages are normalized against the corresponding injected current. For both surface and
 293 borehole electrodes the normalized voltage distribution can be compared against the one expected from the solution for a single
 294 current electrode, idealized as a point injection of current I at the surface of a homogeneous soil of resistivity ρ :

$$295 \quad V = \frac{I\rho}{2\pi r} \quad , \quad (4)$$

296 where r is the distance between the (surface) injection point and the point where voltage V is computed (see Fig.5e for a
 297 comparison). In all cases, both for surface and borehole electrodes, and both for stem and soil current injection, the resistance
 298 patterns are deformed with respect to the solution of Eq. (4) for a homogeneous soil. Some pieces of evidence are apparent
 299 from the raw data already:

- 300 a. In all cases, the pattern of surface and subsurface resistance is asymmetric with respect to the injection point (in the
 301 stem or close to it, in the soil) and thus different from the predictions of Eq. (3); this indicates that current pathways
 302 are controlled by the soil heterogeneous structure: note that at all times there is a clear indication that a conductive
 303 pathway extends from the plant to the right-upper corner of the image (this would be the classical use of MALM –
 304 identifying the shape of conductive bodies underground). Note that spatial variations of resistance between boreholes
 305 are consistent with surface observations i.e. the maximum resistance was measured on the borehole 4 located in the
 306 top right corner of the plot;
- 307 b. The resistance patterns in the case of stem injection are clearly different from the corresponding ones obtained from
 308 soil injection. In particular, injecting in the soil directly produces a stronger resistance signal both at the surface and
 309 in the boreholes than the corresponding resistance in the case of stem injection: this difference clearly points towards
 310 the fact that the plant-roots system must convey the current in a different way than the soil alone; tentatively the
 311 observed resistance features would indicate a deeper current injection in the case of stem injection. Looking at the
 312 qualitative differences between soil and stem injection in the borehole electrode data, the impact is very small at
 313 depths larger than 0.6m;
- 314 c. For both soil and stem injection, local anomalies observed in the background image are either removed or smoothed
 315 during the irrigation steps. The effect is equally pronounced in soil and stem injection, showing that this is caused
 316 essentially by the change in resistivity induced by the change in soil water content (see Fig.5).

317 Similar features are observed for plant A (results shown in appendix C1 and C2). The full-time monitoring is also shown only
 318 in appendix since a consistent and quantitative interpretation is not straightforward by a visual inspection of the raw MALM
 319 data.

320 3.3 Inversion of virtual current sources to estimate roots extents

321 Figure 6 shows the iso-surfaces of fitness index (or misfit) F_I (Eq. 2) for the background (pre-irrigation) conditions of plant B
 322 (plant A in appendix C3) and for current injection in the soil and in the stem at all-time steps listed in Table 1. In all cases,
 323 Figure 6 shows the iso-surface corresponding to the value $F_I = 7V$ corresponding to the 25% misfit index (value selected after

324 analysing the evolution of the L-curve of sorted misfit F_I . The same threshold is fixed for all the time steps thus the images
325 provide comparable information for all cases. Note, nevertheless, that the position of the active roots from one acquisition to
326 the other during the irrigation experiment (or for different seasons) may vary, so the distribution of the misfit and ultimately
327 the depth of the iso-surface describing active roots.

328 In particular, the F_I procedure highlights the remarkable difference, for both plants A and B, between the injection in the stem
329 and in the soil. Current injection in the soil produces a voltage distribution that, albeit corresponding to a heterogeneous
330 resistivity distribution and thus different from the predictions of a simpler model such as Eq. (3), collapses effectively to one
331 point, i.e. the point where current was effectively injected in the ground. On the contrary, when current is injected in the stem,
332 the region of possible source locations in the ground is much wider, and depicts a volume that is likely to correspond to the
333 contact points between roots and soil, i.e. the volume where roots have an active role in the soil especially in terms of RWU.
334 While this latter interpretation remains somewhat speculative, at least in the present experimental context, nevertheless the
335 different results between soil and stem injection can only find an explanation in the role of roots and their spatial structure.
336 The most interesting feature shown by Fig. 6 is that the likely source volumes do not change with time during irrigation except
337 for the irrigation time T_1 for which the iso-surface extended slightly more at depth. Note that the F_I procedure makes use of
338 the changing electrical resistivity distributions caused by infiltrating water (see Fig.4) thus the result is not obvious, and
339 indicates an underlying mechanism that is likely to be linked to the permanence of the roots structure over such a short time
340 lapse.

341 Figure 7 shows the spatial distribution of the current density as an outcome of the minimisation of the F_2 function. Very similar
342 observations to F_I are driven from the current source density i.e. that current injection in the soil produces a current distribution
343 collapses effectively to one point, i.e. the point where current was effectively injected in the ground, while when current is
344 injected in the stem, the current distribution in the ground is much wider, and depicts a volume that is likely to correspond to
345 the contact points between roots and soil. Note that the different time steps (Fig. C4) did not highlight changes in the
346 distribution of current density suggesting that the region of RWU was relatively constant during the experiment.

347 **3.4 Electrical resistivity variations inside and outside the likely active roots zone**

348 Our assumption is that the region identified by MALM F_I for the background time corresponds to the RWU region. The inner
349 area (IN) is then defined as the area within the closed iso-surface at the background time T_0 . As the changes in the estimated
350 extent of the root zone are only minor (Fig. 6), it makes sense to evaluate the changes, as an effect of irrigation, in electrical
351 resistivity within such stable estimated root zone. Figure 8 shows the ER variations of selected values in the zones outside and
352 inside this estimated active root zone. It is apparent how irrigation causes a general decrease of electrical resistivity for both
353 plants A (Fig. 8a) and B (Fig. 8b), and in both inner and outer regions. Note that even though the regions are different for the
354 two plants, the behaviour is similar. Then at the end of irrigation we observe, for both plants, that resistivity continues to
355 decrease outside the root active region, while it increases slightly inside. This behaviour is consistent with the fact that inside
356 the region we expect that RWU progressively dries the soil, while outside this region resistivity continues to decrease (overall)
357 as an effect (probably) of water redistribution in the unsaturated soil.

358 **3.5 One-dimensional simulation of the infiltration**

359 Figure 9a shows, the variations of the simulated soil water content (θ_{simu}) with time for control points located at different depths
360 (see Fig. 2 for the geometry) and Fig. 9b shows the comparison against the 3dimensional variations of ER transformed values
361 to soil water content (θ_{ERT}). Time steps of the ERT acquisition for starting time and end time are reported on Fig. 9a for an
362 easier comparison with Fig. 9b. At T_0 , values of soil water content are about 0.1, a value close to field capacity for this type of
363 soil, as previously assumed (section 2.2) and in agreement with the literature. Despite all the assumptions and models'

364 limitation described later, the range of soil water seems also consistent between the simulation and the measured data. Note
365 also that the dynamic is closely linked to the estimated ET and mean air temperature shown in Figure 2. The start and end time
366 of the triggered irrigation are clearly identified respectively with a sharp increase following by a decrease of θ_{simu} at $z=0$, with
367 a peak in SWC equal to 0.3. Between T_1 and T_2 , only the upper surface ($<0.2\text{m}$ depth) is affected by the irrigation front resulting
368 in the increase of soil water content both visible in θ_{simu} and θ_{ERT} (Fig. 9b). The infiltration front reaches the depth of 0.4 m
369 during the collection of ERT data at time T_2 . Time T_2 marks the starts of a regular decrease of the soil water content overnight
370 in the top 40cm soil. Time T_3 , coincident with an increasing ET and mean air temperature, highlights a rupture from a slow
371 decrease to a higher decrease rate particularly for the soil surface (the layer $<0.2\text{m}$ depth), in agreement with the observed
372 changes in θ_{ERT} (Fig. 9b). Overall, Fig. 9a and 9b show a good correlation between the dynamics of SWC changes predicted
373 by the hydrological model (θ_{simu}) and observed via the ER transformed values (θ_{ERT}).

374 **4 Discussion**

375 The survey was carried out during a sunny summer season in a non-irrigated vineyard of the Bordeaux Region. The site is
376 composed of sandy-loamy soil, thus there is a high infiltration rate during the experiment, and this would make it more difficult
377 to distinguish RWU zones from infiltration zones as done for instance by Cassiani et al. (2015) using time-lapse ERT alone.
378 The first objective of the study was to define a non-invasive investigation protocol capable of “imaging” the root activity as
379 well as the distribution of active roots under varying soil water content. We demonstrated that the key additional information
380 is provided by MALM which directly incorporates the ERT information in terms of changing electrical resistivity distribution
381 in space including its evolution in time. MALM, and particularly its double application of current injection in the stem and in
382 the soil next to it, uses electrical measurements in a totally different manner: here the plant-root system itself acts as a
383 conductor, and the goal is to use the retrieved voltage distribution to infer where the current injected in the stem actually is
384 conveyed into the soil: these locations are potentially the same locations where roots interact with the soil in terms of RWU.
385 However, in order to try and locate the position of these points, it is necessary to know the soil electrical resistivity distribution
386 at the time of measurements. At this scale of measurements, ERT provides 3D images of electrical resistivity distribution in
387 the subsoil housing the root system. Fast acquisition allows the measurement of resistivity changes over time, which in turn
388 can be linked to changes in SWC. This can be caused e.g. by water infiltration, or by RWU: in the latter case, negative SWC
389 changes mapped through resistivity changes can be used to map the regions where roots exert an active suction and reduce
390 SWC. However, water redistribution in the soil also plays a role in terms of resistivity changes. Thus some additional
391 independent information about the location of active roots in the soil may help: this is the first coupling between ERT and
392 MALM that has been integrated in the workflow. Considering the inverted MALM data as non-sensitive to soil water
393 distribution has different potential useful impacts: the separation of contributions of root zone and outer area on ER values
394 extracted from ERT help distinguish between soil processes such as RWU and hydraulic redistribution (hydraulic lift in
395 particular).

396 Time-lapse ERT measurements gives clear evidence that injecting current in the stem and in the soil close to the stem produces
397 different inversions even under changing soil water conditions. The soil injection produces a current density close to a punctual
398 injection (located at the true single electrode location) whatever the soil water content. The stem injection helps identify a 3D
399 region of likely distributed current injection locations, thus defining a region in the subsoil where RWU is likely to take place.
400 The latter result is particularly useful, in perspective: when computing the time-lapse changes of electrical resistivity inside
401 and outside this tentative RWU region during irrigation we clearly see that while inside resistivity increases (as an effect of
402 RWU, as irrigation is still ongoing), outside resistivity decreases. Thus, our assumption that the region identified by MALM
403 inversion (albeit very rough) corresponds to the RWU region is corroborated indirectly also by this evidence.

404

405 **4.1 Comparison between geophysical data and hydrological model**

406 A second objective of the study was to integrate the geophysical results in a simple 1D model of the infiltration experiment,
407 that takes into account the observed water fluxes. Dupuy et al., (2010) advocated the use of roots systems described as “density”
408 distributions. We assimilated the root distribution, derived the geophysical data, into the hydrological model. Attempts in this
409 direction are very promising to describe the root functioning in the framework of continuum physics, i.e. the one endorsed by
410 SPAC. The integration of modelling and data has proven a key component of this type of hydro-geophysical studies, allowing
411 us to draw quantitative results of practical interest. For example, in our study it is apparent that although infiltration occurred
412 during the peak of evapotranspiration (between 1pm and 3pm), very small RWU was observed before the second day.
413 Nevertheless, after a certain time, RWU is observed while infiltration is still ongoing. Smaller RWU observed for the small
414 plant A compared to plant B is also observed.

415 **4.2 Recommendation for future experiments**

416 In this field case study, we had very little available quantitative information that could allow the validation of the geophysical
417 data in terms of the volume of soil affected by RWU. The final objective of this study was then to discuss issues for obtaining
418 suitable validation data using existing methods and propose some recommendation for future experiments:

- 419 (i) Traditional root sampling methods should be the first line of validation although they have numerous potential
420 pitfalls. As roots are underground, and thus invisible in their space-time evolution, and are also fragile, especially
421 in their fine structure, the monitoring of their structure and activity using destructive methods such as trenches
422 or air spade presents various limitations. In such approaches, even in the best case where fine roots may be
423 sufficiently preserved and described, it is impossible to know where the active roots actually are. Active roots
424 may be located only in one part of the whole root system. Destructive methods may help to validate the
425 confidence area determined by F_1 but are not appropriated methods to validate the F_2 inversion.
- 426 (ii) We recommend the use of traditional methods (such as Time Domain Reflectometry-TDR and tensiometers) for
427 future studies. Though punctual, these data can greatly facilitate the data calibration and validation of geophysical
428 methods.

429 Finally, more research needs to be conducted to understand how MALM can provide information to be correlated with the
430 actual RWU and thus to the estimated transpiration. The study of complex root-soil interactions requires that high time
431 resolution and extensive data are collected and processed. In order to quantitatively evaluate RWU using the variations of ER,
432 many more data instants per day must be acquired. In this study, we only used ERT and MALM information to initialize the
433 infiltration model, and only a qualitative comparison was conducted between model predictions and geophysical results. In the
434 near future, a real assimilation scheme using data assimilation technique should be adopted.

435 **5 Conclusions**

436 This study presents an approach to define the extent of active roots distribution using non-invasive investigations, and thus
437 particularly suitable to be applied under real field conditions. We applied a mix of ERT and MALM techniques, using the
438 same electrode and surface electrode distribution. The power of the approach lies in the complementary capabilities of the two
439 techniques in providing information concerning the root structure and activity. The approach has been tested in a vineyard
440 during an irrigation experiment. Future experiments would require that high time resolution extensive data are collected, and
441 the results are analysed in conjunction with data from traditional monitoring methods in order to qualitatively integrate
442 geophysical results into a hydrological one. The presented approach can be easily replicated under a variety of conditions, as
443 DC electrical methods such as ERT and MALM do not possess a spatial scaling per se, but their resolution depends on electrode

444 spacing as well as on other factors that are difficult to assess a priori, such as resistivity contrasts and signal to noise ratio.
445 Thus similar experiments can also be used in the laboratory, where more direct evidence of root distribution can be used to
446 further validate the method.

447 **Acknowledgements**

448 The authors wish to acknowledge support from the ERANET-MED project WASA ("Water Saving in Agriculture:
449 Technological developments for the sustainable management of limited water resources in the Mediterranean area"). The
450 authors from the University of Padua acknowledge support also from the University Research Project "Hydro-geophysical
451 monitoring and modelling for the Earth's Critical Zone" (CPDA147114). In addition, the information, data or work presented
452 herein was funded in part by the Department of Energy Advanced Research Projects Agency-Energy (ARPA-E) project under
453 work authorization number 16/CJ000/04/08 and Office of Science Biological and Environmental Research Watershed
454 Function SFA project under Contract Number DE-AC02-05CH11231. The views and opinions of authors expressed herein do
455 not necessarily state or reflect those of the United States Government or any agency thereof. Luca Peruzzo and Myriam
456 Schmutz gratefully acknowledge the financial support from IDEX (Initiative D'EXcellence, France), the European regional
457 development fund Interreg Sudoe – Soil Take Care, no. SOE1/P4/F0023 – Sol Precaire.

458 **Data availability**

459 Data used to generate the figures can be accessed on the Padua Research Archive ([Link to come after decision](#)).
460

461 **Authors contributions**

462 GC, YW, and SH worked on the conceptualization of the research. BM curated the data. LP, BM, NC and JB collected the
463 data. BM prepared the formal analysis, designed and wrote the scripts for carrying out the simulation and inversion, and ran
464 the obtained the results. MS and GC supervised the field work. All the authors discussed the results. BM prepared the paper
465 with contributions from all the authors.

466 **Competing interests**

467 The authors declare that they have no conflict of interest.

468 **References**

- 469 Amato, M. *et al.* Multi-electrode 3d resistivity imaging of alfalfa root zone. *Eur. J. Agron.* 31, 213–222 (2009).
470 Anderegg W.R.L, J.M. Kane and L.D.L. Anderegg, 2013, Consequences of widespread tree mortality triggered by drought
471 and temperature stress, *Nature Climate Change*, 3(1), 30-36, doi: 10.1038/nclimate1635.
472 Archie, G. E. The electrical resistivity log as an aid in determining some reservoir characteristics. *Transactions AIME* 146,
473 54–62 (1942).
474 Band L.E., J.J. McDonnell, J.M. Duncan, A. Barros, A. Bejan, T. Burt, W.E. Dietrich, R.E. Emanuel, T. Hwang, G. Katul, Y.
475 Kim, B. McGlynn, B. Miles, A. Porporato, C. Scaife, P.A. Troch, 2014, Ecohydrological flow networks in the subsurface,
476 *Ecohydrology*, 7(4), 1073-1078, doi: 10.1002/eco.1525.
477 Binley, 2019, A. R3t version 1.9. *User Guide. University of Lancaster, UK.*

478 Binley, A. and A. Kemna, 2005, DC resistivity and induced polarization methods. In *Hydrogeophysics*, 129–156, Springer.

479 Brovelli A. and G. Cassiani, 2011, Combined estimation of effective electrical conductivity and permittivity for soil
480 monitoring, *Water Resources Research*, 47, W08510, doi:10.1029/2011WR010487.

481 Brillante, L., Mathieu, O., Bois, B., van Leeuwen, C. and Lévêque, J.: The use of soil electrical resistivity to monitor plant and
482 soil water relationships in vineyards, *SOIL*, 1(1), 273–286, doi:10.5194/soil-1-273-2015, 2015.

483 Campbell, R. B., Bower, C. A., and Richards, L. A., 1949, Change of Electrical Conductivity With Temperature and the
484 Relation of Osmotic Pressure to Electrical Conductivity and Ion Concentration for Soil Extracts, *Soil Sci. Soc. Am. J.*,
485 13, 66, doi: 10.2136/sssaj1949.036159950013000C0010x.

486 Cassiani, G., Bruno, V., Villa, A., Fusi, N. and A.M. Binley, 2006, A saline trace test monitored via time-lapse surface
487 electrical resistivity tomography. *J. Appl. Geophys.* 59, 244 – 259, doi: 10.1016/j.jappgeo.2005.10.007.

488 Cassiani, G., Ursino, N., Deiana, R., Vignoli, G., Boaga, J., Rossi, M., Perri, M. T., Blaschek, M., Duttmann, R., Meyer, S.,
489 Ludwig, R., Soddu, A., Dietrich, P., and Werban, U., 2012, Noninvasive Monitoring of Soil Static Characteristics and
490 Dynamic States: A Case Study Highlighting Vegetation Effects on Agricultural Land, *Vadose Zone J.*, 11, 3,
491 <https://doi.org/10.2136/vzj2011.0195>.

492 Cassiani, G., Boaga, J., Vanella, D., Perri, M. T. & Consoli, S. Monitoring and modelling of soil-plant interactions: the joint
493 use of ert, sap flow and eddy covariance data to characterize the volume of an orange tree root zone. *Hydrol. Earth Syst.*
494 *Sci.* 19, 2213–2225, DOI: 10.5194/hess-19-2213-2015 (2015).

495 Cassiani G., J. Boaga, M. Rossi, G. Fadda, M. Putti, B. Majone, A. Bellin, 2016, Soil-plant interaction monitoring: small scale
496 example of an apple orchard in Trentino, North-Eastern Italy, *Science of the Total Environment*, Vol. 543, Issue Pt B, pp.
497 851-861, doi: 10.1016/j.scitotenv.2015.03.113.

498 Chahine M.T., 1992, The hydrological cycle and its influence on climate, *Nature*, 359, 373-380, doi: 10.1038/359373a0

499 Consoli S., F. Stagno, D. Vanella, J. Boaga, G. Cassiani, G. Rocuzzo, 2017, Partial root-drying irrigation in orange orchards:
500 effects on water use and crop production characteristics, *European J. of Agronomy*, Volume 82, 190-202, doi:
501 10.1016/j.eja.2016.11.001.

502 Couvreur V., J. Vanderborght and M. Javaux, 2012, A simple three-dimensional macroscopic root water uptake model based
503 on the hydraulic architecture approach, *Hydrol. Earth Syst. Sci.*, 16(80), 2957-2971, doi: 10.5194/hess-16-2957-2012

504 Dalton, F. N., 1995, In-situ root extent measurements by electrical capacitance methods, *Plant Soil*, 173, 157–165, doi:
505 10.1007/BF00155527.

506 Dawson T.D. and R.T.W. Siegwolf (eds), 2007, Stable Isotopes as Indicators of Ecological Change, *Terrestrial Ecology Series*,
507 *Elsevier*, 417 pp.

508 de Arellano J.V.G., C.C. van Heerwaarden, J. Levievel, 2012, Modelled suppression of boundary-layer clouds by plants in a
509 CO₂-rich atmosphere, *Nature Geoscience*, 5(10), 701-704, doi: 10.1038/NGEO1554.

510 De Carlo L., M.T. Perri, M.C. Caputo, R. Deiana, M. Vurro and G. Cassiani, 2013, Characterization of the confinement of a
511 dismissed landfill via electrical resistivity tomography and mise-à-la-masse, *Journal of Applied Geophysics*, 98 (2013)
512 1–10, doi: 10.1016/j.jappgeo.2013.07.010.

513 Dirmeyer P.A., R.D. Koster and Z. Guo, 2006, Do global models properly represent the feedback between land and
514 atmosphere? , *J. of Hydrometeorology*, 7(6), 1177-1198, doi: 10.1175/JHM532.1.

515 Dirmeyer, P. A., E. K. Jin, J. L. Kinter III and J. Shukla, 2014: Land Surface Modeling in Support of Numerical Weather
516 Prediction and Sub-Seasonal Climate Prediction. *White Paper: Workshop on Land Surface Modeling in Support of NWP*
517 *and Sub-Seasonal Climate Prediction*, 17pp.

518 Draye X., Y. Kim, G. Lobet and M. Javaux, 2010, Model-assisted integration of physiological and environmental constraints
519 affecting the dynamic and spatial patterns of root water uptake from soils, *J. of Experimental Botany*, 61(8), 2145-2155,
520 doi: 10.1093/jxb/erq077.

521 Dupuy L., M. Vignes, B.M. McKenzie and P.J. White, 2010, The dynamics of root meristem distribution in the soil, *Plant,*
522 *Cell and Environment*, 33(3), 358-369, doi: 10.1111/j.1365-3040.2009.02081.x.

523 Dupuy L., T. Fourcaud, A. Stokes and F. Danion, 2005, A density-based approach for the modelling of root architecture:
524 application to Maritime pine (*Pinus pinaster* Ait.) root systems, *J. of Theoretical Biology*, 3, 323-334, doi:
525 10.1016/j.jtbi.2005.03.013.

526 Dupuy L. and M. Vignes, 2012, An algorithm for the simulation of the growth of root systems on deformable domains, *J. of*
527 *Theoretical Biology*, 310, 164-174, doi: 10.1016/j.jtbi.2012.06.025.

528 Garré, S., Javaux, M., Vanderborght, J., Pagès, L. & Vereecken, H., 2011, Three-dimensional electrical resistivity tomography
529 to monitor root zone water dynamics. *Vadose Zone J.* 10, 412–424 doi: 10.2136/vzj2010.0079.

530 Gerwitz A. and E.R. Page, 1974. Empirical Mathematical - Model to Describe Plant Root Systems 1. *Journal of Applied*
531 *Ecology*, 11, 773-781.

532 Gibert, D., Le Mouël, J.-L., Lambs, L., Nicollin, F., and Perrier, F., 2006, Sap flow and daily electric potential variations in a
533 tree trunk, *Plant Sci.*, 171, 572–584, doi: 10.1016/j.plantsci.2006.06.012.

534 Hackett C. and D.A. Rose, 1972, A model of the extension and branching of a seminal root of barley, and its use in studying
535 relations between root dimensions. I. The model. *Aust. J. Biol. Sci.*, 25, 669–679.

536 Jourdan C. and H. Rey, 1997, Modelling and simulation of the architecture and development of the oil-palm (*Elaeis guineensis*
537 Jacq) root system .1. The model, *Plant and Soil*, 190(2), 217-233, doi: 10.1023/A:1004218030608

538 Kemna A., A. Binley, G. Cassiani, E. Niederleithinger, A. Revil, L. Slater, K. H. Williams, A. Flores Orozco, F.-H. Haegel,
539 A. Hördt, S. Kruschwitz, V. Leroux, K. Titov, E. Zimmermann, 2012, An overview of the spectral induced polarization
540 method for near-surface applications, *Near Surface Geophysics*, doi: 10.3997/1873-0604.2012027.

541 Mary, B., G. Saracco, L. Peyras, M. Vennetier, P. Mériaux and C. Camerlynck, 2016, Mapping tree root system in dikes using
542 induced polarization: Focus on the influence of . *J. Appl. Geophys.* 135, 387 – 396, doi:
543 <https://doi.org/10.1016/j.jappgeo.2016.05.005>.

544 Mary, B., F. Abdulsamad, G. Saracco, L. Peyras, M. Vennetier, P. Mériaux and C. Camerlynck 2017, Improvement of coarse
545 root detection using time and frequency induced polarization: from laboratory to field experiments. *Plant Soil* 417, 243–
546 259, doi: 10.1007/s11104-017-3255-4.

547 Mary, B., Peruzzo, L., Boaga, J., Schmutz, M., Wu, Y., Hubbard, S. S., and G. Cassiani, 2018, Small scale characterization of
548 vine plant root water uptake via 3D electrical resistivity tomography and Mise-à-la-Masse method, *Hydrol. Earth Syst.*
549 *Sci.* , doi: 10.5194/hess-22-5427-2018.

550 Mary, B., Vanella, D., Consoli, S. and Cassiani, G.: Assessing the extent of citrus trees root apparatus under deficit irrigation
551 via multi-method geo-electrical imaging, *Sci Rep*, 9(1), 9913, doi:10.1038/s41598-019-46107-w, 2019a.

552 Maxwell R.M, F.K. Chow and S.J. Kollet, 2007, The groundwater-land-surface-atmosphere connection: Soil moisture effects
553 on the atmospheric boundary layer in fully-coupled simulations, *Advances in Water Resources*, 30(12), 2447-2466, doi:
554 10.1016/j.advwatres.2007.05.018.

555 Manoli G., S. Bonetti, J.C. Domec, M. Putti, G. Katul and M. Marani, 2014, Tree root systems competing for soil moisture in
556 a 3D soil-plant model, *Advances in Water Resources*, 66, 32–42, doi: 10.1016/j.advwatres.2014.01.006.

557 Michot, D., Benderitter, Y., Dorigny, A., Nicoullaud, B., King, D., and Tabbagh, A., 2003, Spatial and temporal monitoring
558 of soil water content with an irrigated corn crop cover using surface electrical resistivity tomography: soil water study
559 using electrical resistivity, *Water Resour. Res.*, 39, doi: 10.1029/2002WR001581.

560 Michot, D., Thomas, Z. and Adam, I.: Nonstationarity of the electrical resistivity and soil moisture relationship in a
561 heterogeneous soil system: a case study, *SOIL*, 2(2), 241–255, doi:10.5194/soil-2-241-2016, 2016.

562 Newman, B. D., Wilcox, B. P., Archer, S. R., Breshears, D. D., Dahm, C. N., Duffy, C. J., McDowell, N. G., Phillips, F. M.,
563 Scanlon, B. R. and Vivoni, E. R.: Ecohydrology of water-limited environments: A scientific vision: OPINION, *Water*
564 *Resour. Res.*, 42(6), doi:10.1029/2005WR004141, 2006.

565 Osiensky, J.L., 1997. Ground water modeling of mise-a-la-masse delineation of contaminated ground water plumes. *J. Hydrol.*
566 197 (1–4), 146–165. doi: 10.1016/S0022-1694(96)03279-9.

567 Parasnis, D. S., 1967, Three-dimensional electric mise-a-la-masse survey of an irregular lead-zinc-copper deposit in central
568 Sweden, *Geophys. Prospect.* 15, 407–437, doi: 10.1111/j.1365-2478.1967.tb01796.x.

569 Perri M.T., P. De Vita, R. Masciale, I. Portoghese, G.B. Chirico and G. Cassiani, 2018, Time-lapse Mise-à-la-Masse
570 measurements and modelling for tracer test monitoring in a shallow aquifer, *Journal of Hydrology*, 561, 461-477, doi:
571 10.1016/j.jhydrol.2017.11.013

572 Peruzzo, L., 2019, Thesis, Approches géoélectriques pour l'étude du sol et d'interaction sol-racines. Bordeaux 3,
573 <http://www.theses.fr/s141626>

574 Philip J.R., 1966, Plant Water Relations: Some Physical Aspects, *Annual Review of Plant Physiology*, 17, 245-268.

575 Rao, S., Meunier, F., Ehosioko, S., Lesparre, N., Kemna, A., Nguyen, F., Garré, S. and Javaux, M.: Impact of Maize Roots on
576 Soil-Root Electrical Conductivity: A Simulation Study, *Vadose Zone Journal*, 18(1), 190037,
577 doi:10.2136/vzj2019.04.0037, 2019.

578 Rhoades, J. D., Raats, P. A. C., and Prather, R. J., 1976, Effects of Liquid-phase Electrical Conductivity, Water Content, and
579 Surface Conductivity on Bulk Soil Electrical Conductivity1, *Soil Sci. Soc. Am. J.*, 40, 651, doi:
580 10.2136/sssaj1976.03615995004000050017x.

581 Richter, D. deB. and Mobley, M. L.: Monitoring Earth's Critical Zone, *Science*, 326(5956), 1067–1068,
582 doi:10.1126/science.1179117, 2009.

583 Schaap, M. G., Leij, F. J. and van Genuchten, M. Th.: rosetta : a computer program for estimating soil hydraulic parameters
584 with hierarchical pedotransfer functions, *Journal of Hydrology*, 251(3–4), 163–176, doi:10.1016/S0022-1694(01)00466-
585 8, 2001.

586 Simunek, J., Sejna, M., Van Genuchten, M. T., Šimůnek, J., Šejna, M., Jacques, D., ... & Sakai, M., 1998, HYDRUS-1D.
587 Simulating the one-dimensional movement of water, heat, and multiple solutes in variably-saturated media, version, 2.

588 Srayeddin, I. and Doussan, C., 2009, Estimation of the spatial variability of root water uptake of maize and sorghum at the
589 field scale by electrical resistivity tomography, *Plant and Soil*, 319, 185–207, doi: 10.1007/s11104-008-9860-5, 2009.

590 Vanella D., G. Cassiani, L. Busato, J. Boaga, S. Barbagallo, A. Binley, S. Consoli, 2018, Use of small scale electrical resistivity
591 tomography to identify soil-root interactions during deficit irrigation, *Journal of Hydrology*, 556, 310-324, doi:
592 10.1016/j.jhydrol.2017.11.025.

593 Volpe V., M. Marani, J.D. Albertson and G. Katul, 2013, Root controls on water redistribution and carbon uptake in the soil-
594 plant system under current and future climate *Adv Water Resour.*, 60, 110-120, doi: 10.1016/j.advwatres.2013.07.008.

595 York L.M., A. Carminati, S.J. Mooney, K. Ritz and M.J. Bennett, 2016, The holistic rhizosphere: integrating zones, processes,
596 and semantics in the soil influenced by roots, *J. Exp. Botany*, 67(12), 3629-3643, doi: 10.1093/jxb/erw108.

597 Waxman, M. H. and Smits, L. J. M., 1968, Electrical Conductivities in Oil-Bearing Shaly Sands, *Soc. Petrol. Eng. J.*, 8, 107–
598 122, doi: 10.2118/1863-A.

599 Weigand, M. and Kemna, A.: Multi-frequency electrical impedance tomography as a non-invasive tool to characterize and
600 monitor crop root systems, *Biogeosciences*, 14(4), 921–939, doi:10.5194/bg-14-921-2017, 2017.

601 Weigand, M. & Kemna, A., 2019, Imaging and functional characterization of crop root systems using spectroscopic electrical
602 impedance measurements. *Plant and Soil*, 435(1-2), 201-224, doi: 10.1007/s11104-018-3867-3.

603 Werban, U., Attia al Hagrey, S., and Rabbel, W., 2008, Monitoring of root-zone water content in the laboratory by 2-D geo-
604 electrical tomography, *J. Plant Nutr. Soil Sc.*, 171, 927–935, doi: 10.1002/jpln.200700145.

606 **Table 1: schedule of the acquisitions and the irrigation times; Plant A and B are measured consecutively and consist each time of**
607 **three measurements: ERT, MALM stem and MALM soil. Assessment of data and inversion quality from the two last columns i.e.**
608 **respectively the percentage of data that passed the reciprocity (analysis at 10%) and RMS error at the end of the inversion.**

Acquisition no.	Plant	Starting time (LT)	Ending time (LT)	Irrigation	Date	% of data retained (10% reciprocals)	Final RMS (Ohm.m)
0 (background)	A	10:20	11:00			79	1.15
	B	12:20	13:00			91	1.76
1 (Irrigation)	A	15:00	15:30	13h00 to 15h30, 104lh-1 For both plants	Day 1 (19 June 2017)	50	1.54
	B	13:30	14:00			68	1.31
2	A	17:00	17:30			69	1.36
	B	18:00	18:45			57	1.50
3	A	10:30	11:00			59	1.72
	B	9:30	10:00			80	1.24
4	A	14:00	14:30		Day 2	72	1.38
	B	15:00	15:30			80	1.53
5	A	18:00	18:30			70	1.23
	B	17:00	17:30			78	1.28

609
610
611

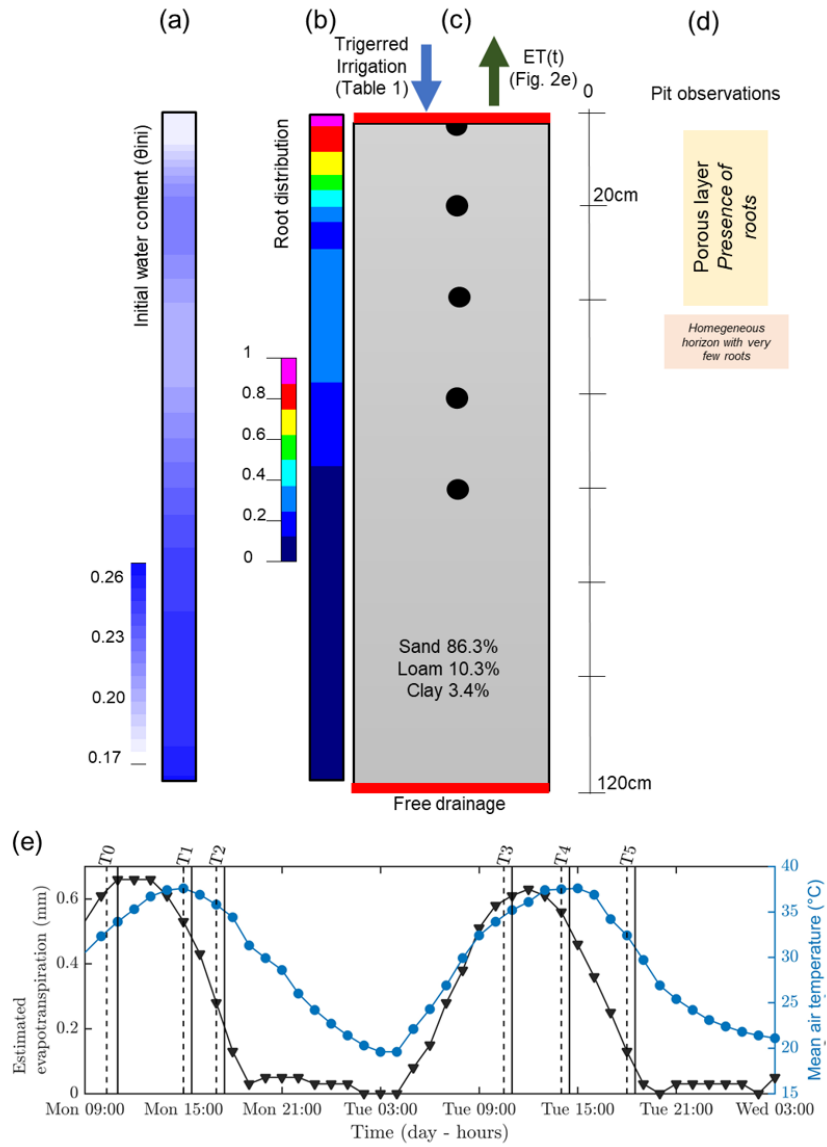


612
613
614
615

Figure 1: picture of the field site in May 2017 (a) wired plants investigated (b) and grape status during the experiment in June 2017 (c)

616

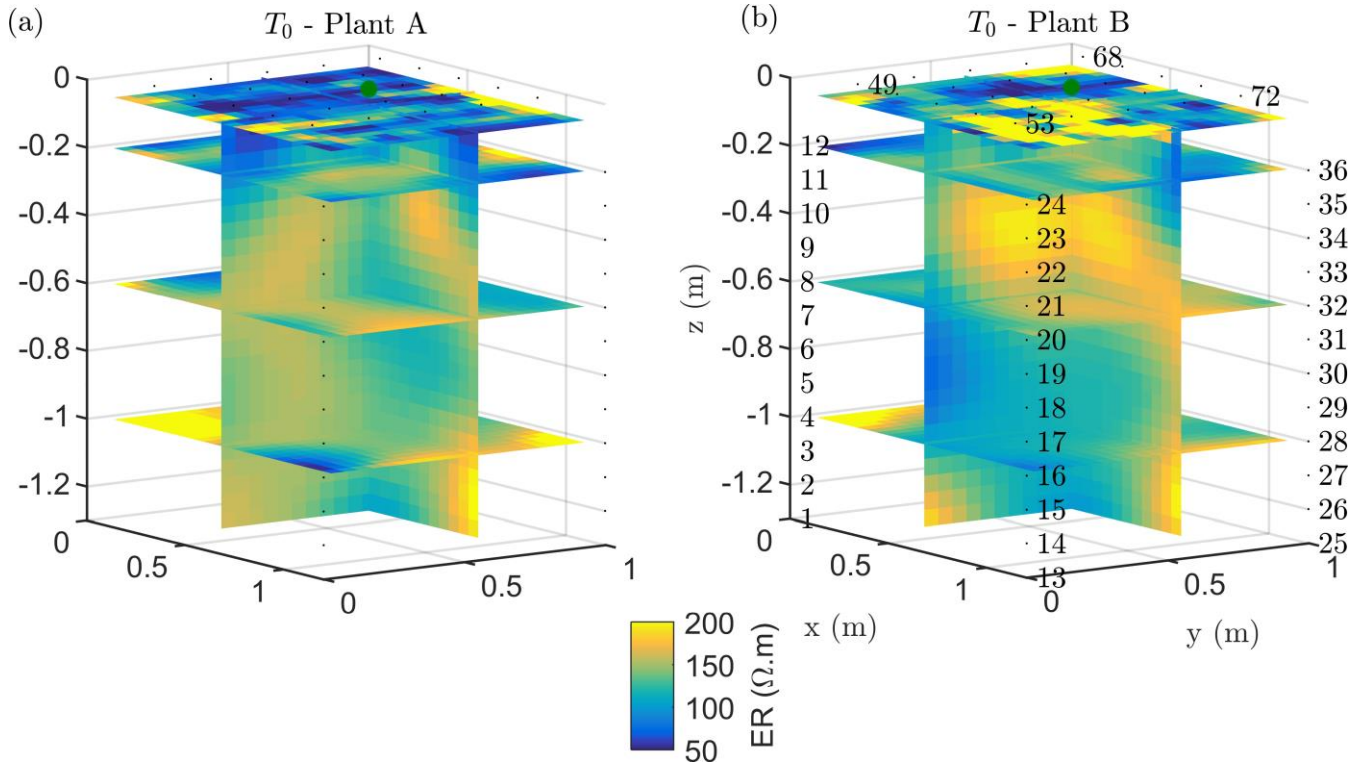
617



618

619 **Figure 2: Initial (a,b,c) and time varying atmospheric conditions (e) used the hydrological simulation (e). From left to right (a-d),**
 620 **initial conditions on soil water content θ_{ini} , root density (1/cm), soil type, and pit observations. (e) variation of temperature (blue line)**
 621 **and estimated evapotranspiration (black line) derived from a nearby meteorological station. The vertical lines indicate acquisition**
 622 **times for plant A (dashed and plain line respectively for the start and the end of the measurement, see Table 1).**

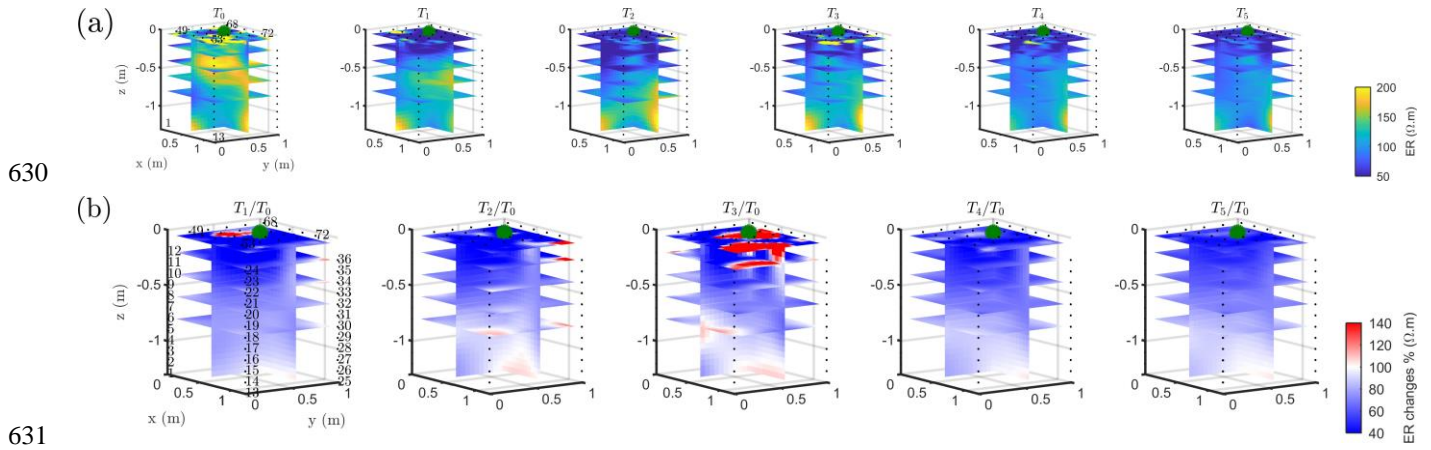
623



625

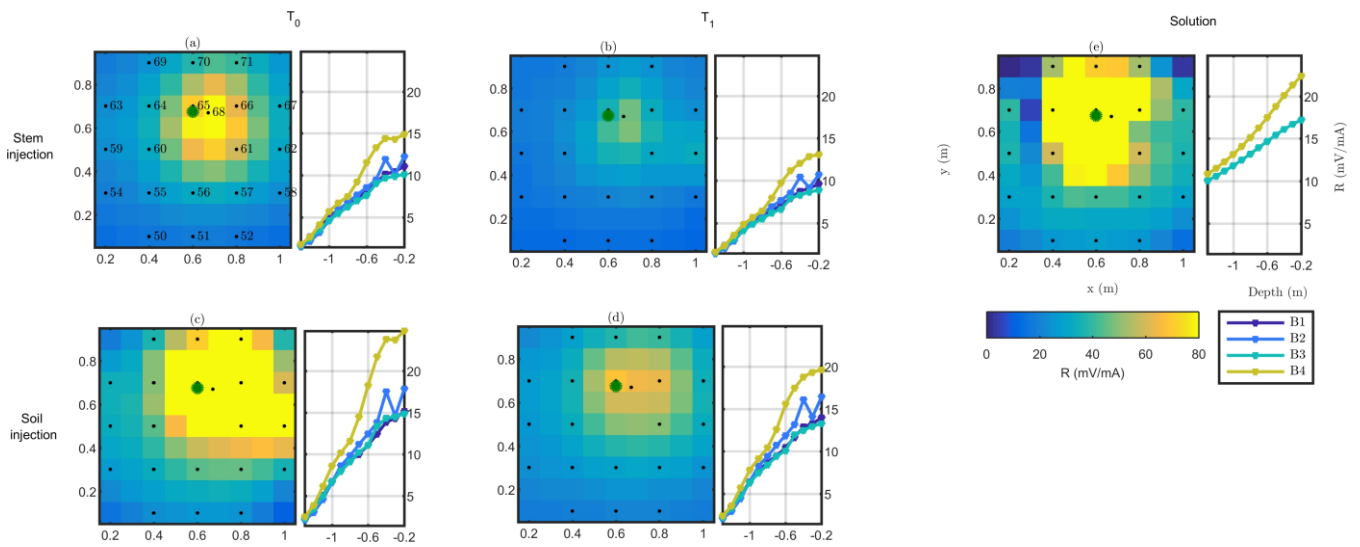
626 **Figure 3: Results of the 3-D ERT inversion for the background time T_0 for plant A (b) and B (b). 3-D resistivity volume (log scale)**
 627 **sliced at the tree stem position (vertically) and at four depths (0.05, 0.2 0.6 and 1m), with the green point showing the location of the**
 628 **plant stem.**

629



633 **Figure 4: 3D ERT results for plant B (plant A, in appendix Fig. B1). The volume is sliced at the tree stem position (vertically) and at**
 634 **five depths (0.05, 0.2, 0.4, 0.6 and 0.8 m). (a) 3D inversion of the resistivity (in Ωm , log scale) from the background time T_0 , during**
 635 **irrigation T_1 and after irrigation. (b) time-lapse inversion (following Cassiani et al., 2006) showing the ratios (in % of ER changes)**
 636 **between time step T_1 and background time T_0 (100% in white means no change).**

637

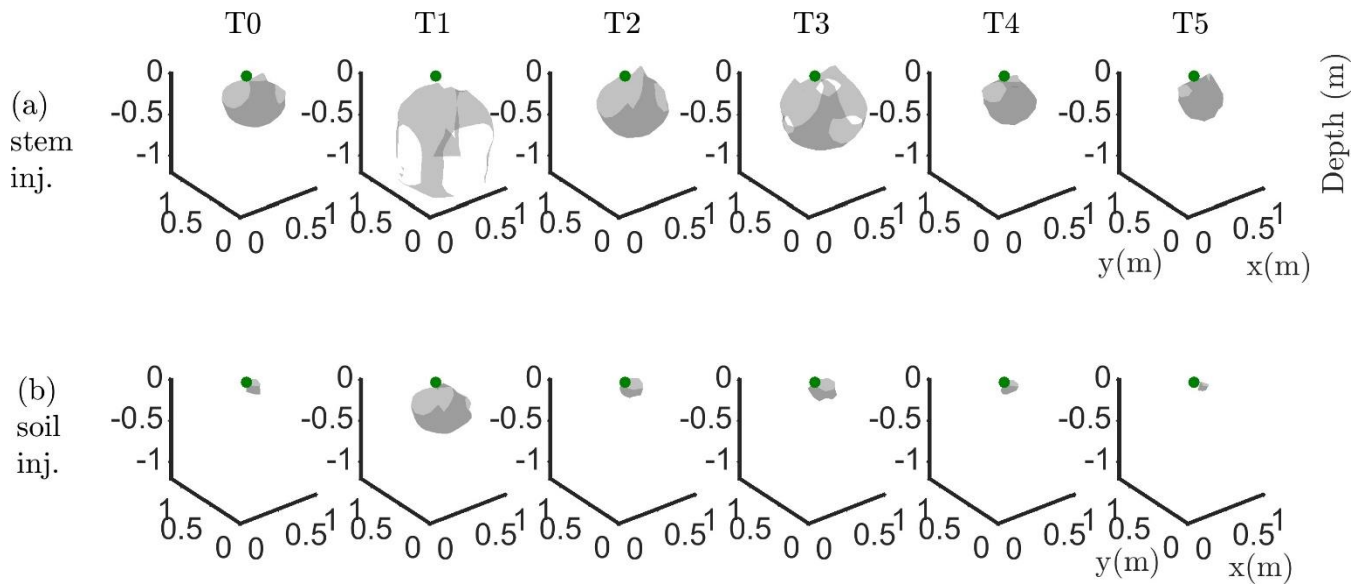


638

639

640 **Figure 5: plant B_A, MALM results showing variations in surface (horizontal plan) of resistance R (in mV/mA) for the initial state**
 641 **background T₀ (a,c) and irrigation T₁ (b,d) time steps. Comparison between the stem injection (a,b) and soil injection (c,d). The**
 642 **black points show the surface electrodes location. The green point shows the positions of the plant stem. Data are filtered using a**
 643 **threshold on reciprocal acquisition of 20%. (e) shows the solution using Eq. (4) for a homogeneous soil of 100 Ohm.m; The resistance**
 644 **between boreholes B1/B3 and B2/B4 (see legend) are identical and cannot be distinguished graphically in the case of (e).**

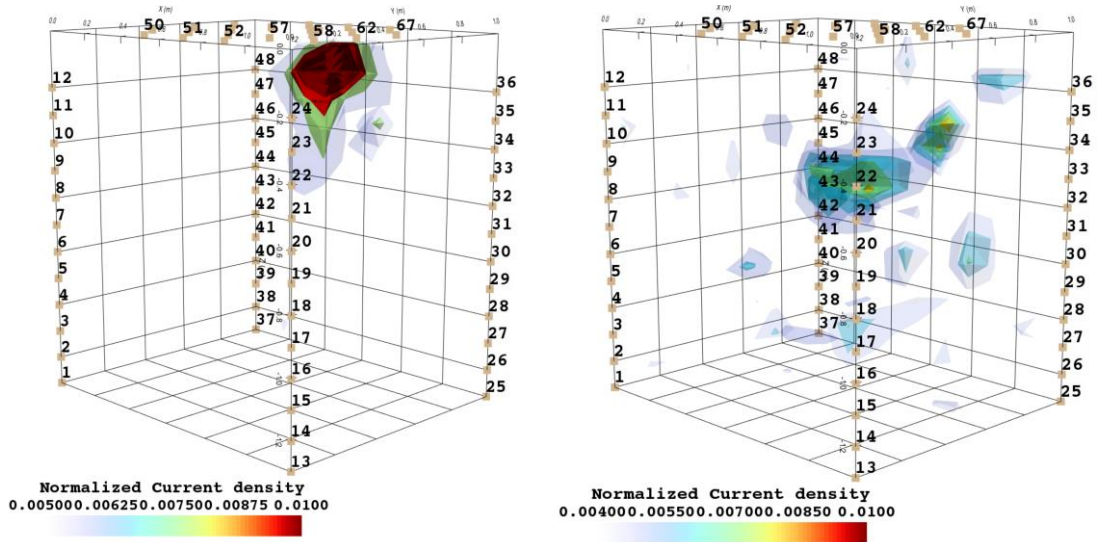
645



647

648 **Figure 6: iso-surface minimizing the F_1 function for plant B; during stem injection (a), during soil injection (b); Columns represent**
 649 **the six times steps from T_0 to T_5 . Green dot shows plant stem position. Threshold is defined by the misfit 25% of the normalised F_1**
 650 **(value selected according to the evolution of the curve of sorted misfit F_1 and calculated for the tree injection at T_0 and kept constant**
 651 **for all the time steps).**

652

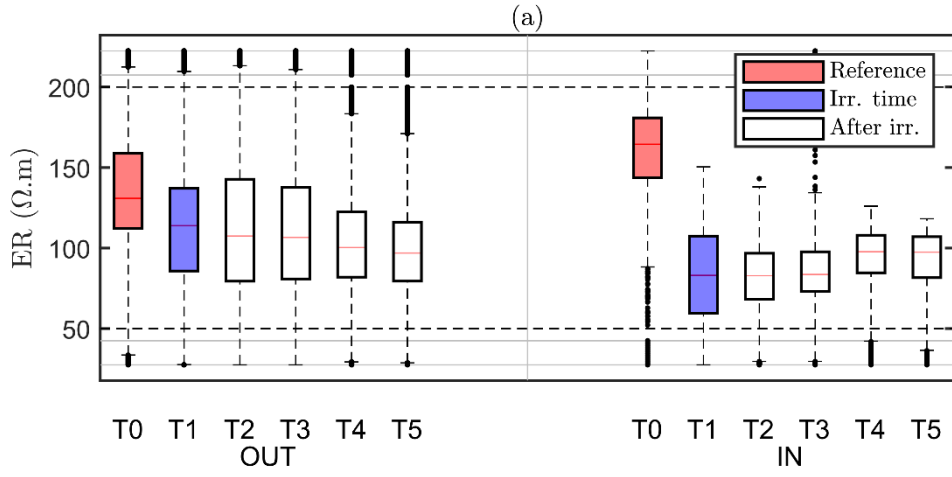


654

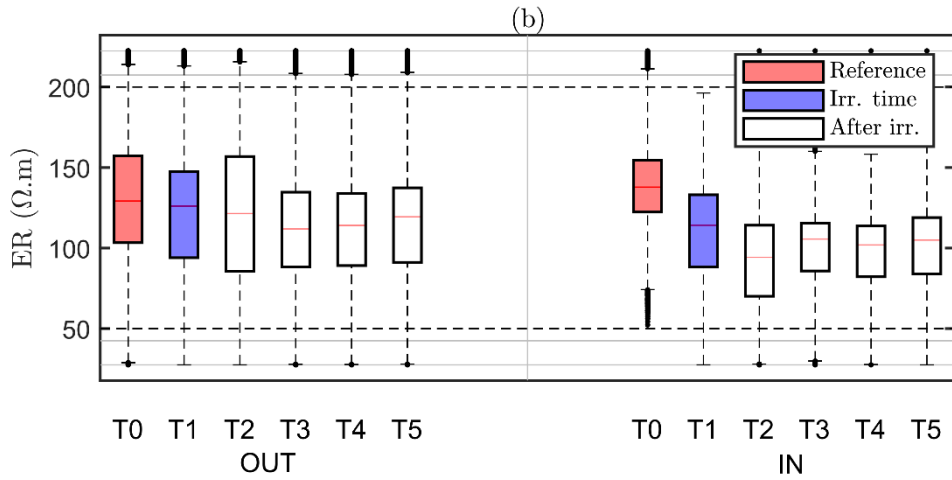
655 **Figure 7: current source density after minimization of the objective function F_2 as defined in Eq. (3). The results are relevant to the**
656 **background time T_0 for the plant B, for the soil current injection (left) and the stem current injection (right).**

657

658



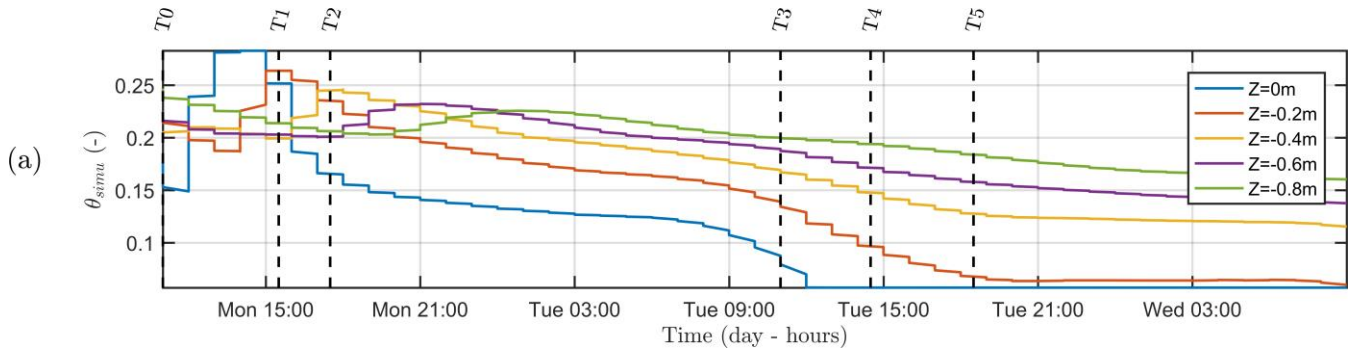
660



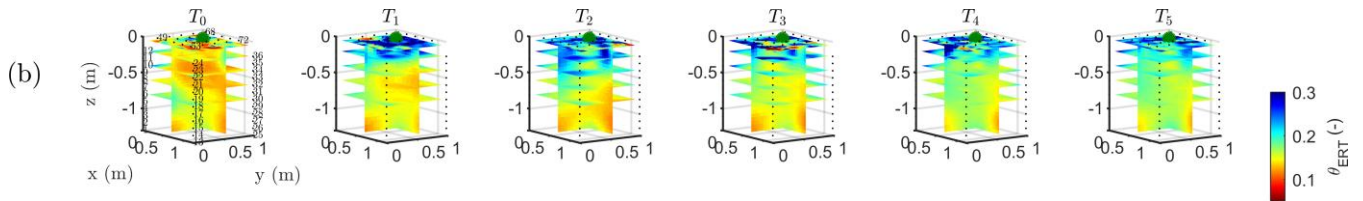
661

662 **Figure 8: boxplot distribution of ER time variations observed on the plant A (top) and plant B (bottom), for the values selected**
 663 **outside (OUT, left part) and inside (IN, right part) of the region defined by the F_1 best fit sources (see Fig. 6a-T₀).** The central mark
 664 **indicates the median, the bottom and top edges of the box indicated the 25th and 75th percentiles of ER data, respectively. The**
 665 **whiskers extend to the most extreme data points (black dots) considered outliers. Each box corresponds to a given time step (see**
 666 **table 1), indicated in the x-axis.**

667



669
670
671
672



673
674
675
676
677

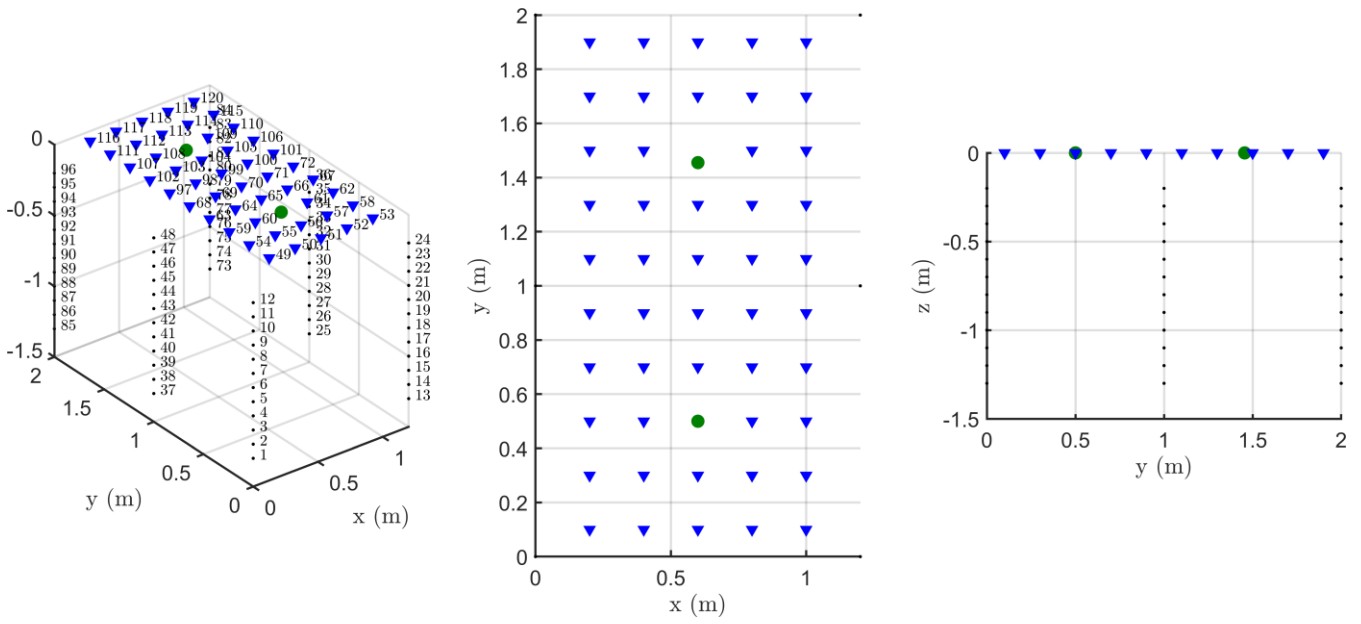
Figure 9: (a) time variation of simulated soil water content (θ_{simu}) at five depths. The vertical lines indicate the geophysical acquisition times (dashed and plain line respectively for the start and the end of the measurement, see Table 1). (b) 3D variations of the ERT-derived soil water content (θ_{ERT}) for the time steps describe in table 1. Horizontal layer depths are identical to the control points of the hydrological model.

678
679

680 **Appendix A: set-up description**

681

682 Fig. A1: from left to right: 3D view of the surface (blue) and borehole (black) electrodes, view from the top and transversal
683 view. Plant A was located downhill. Green dot shows plant stem positions.



684

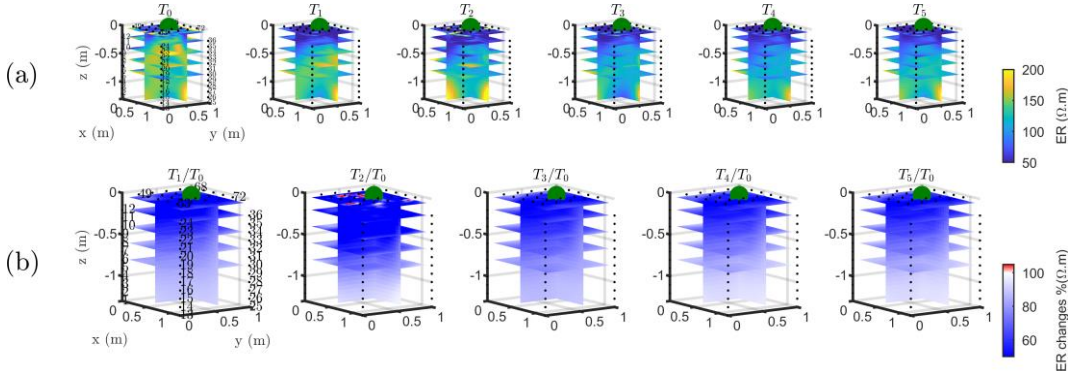
685

686 **Appendix B: ERT monitoring**

687

688 Fig. B1: 3D ERT results for plant A. The volume is sliced at the tree stem position (vertically) and at five depths (0.05, 0.2,
689 0,4, 0.6 and 0.8 m). (a) 3D inversion of the resistivity (in Ωm , log scale) from the background time T_0 , during irrigation T_1 and
690 after irrigation. (b) time-lapse inversion (following Cassiani et al., 2006) showing the ratios (in % of ER changes) between
691 time step T_i and background time T_0 (100% in white means no change).

692



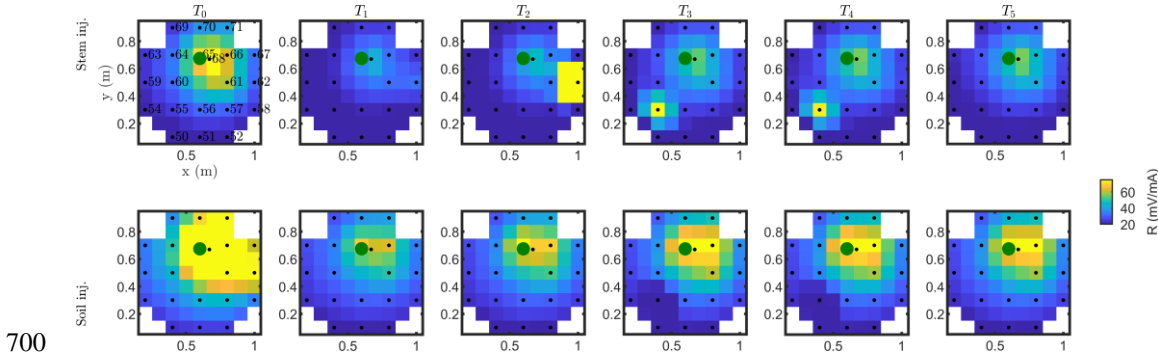
693

694

695 **Appendix C: MALM monitoring**

696

697 Fig. C1: Resistance distribution of the raw data of MALM time lapse monitoring for the plant B. First line results are relevant
698 to the stem injection while second line refers to the soil control injection. Columns describe time evolution according to Table
699 1.

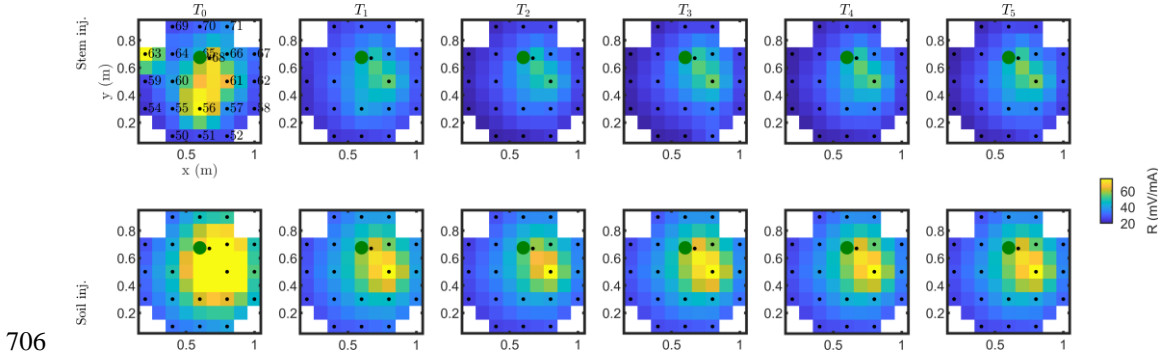


700

701

702

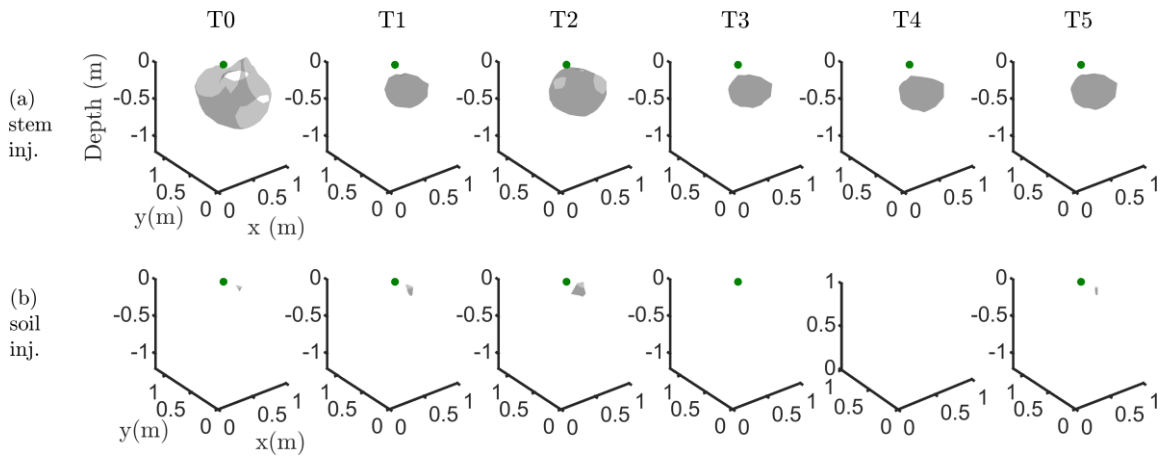
703 Fig. C2: Resistance distribution of the raw data of MALM time lapse monitoring for the plant A. First line results are relevant
704 to the stem injection while second line refers to the soil control injection. Columns describe time evolution according to Table
705 1.



706

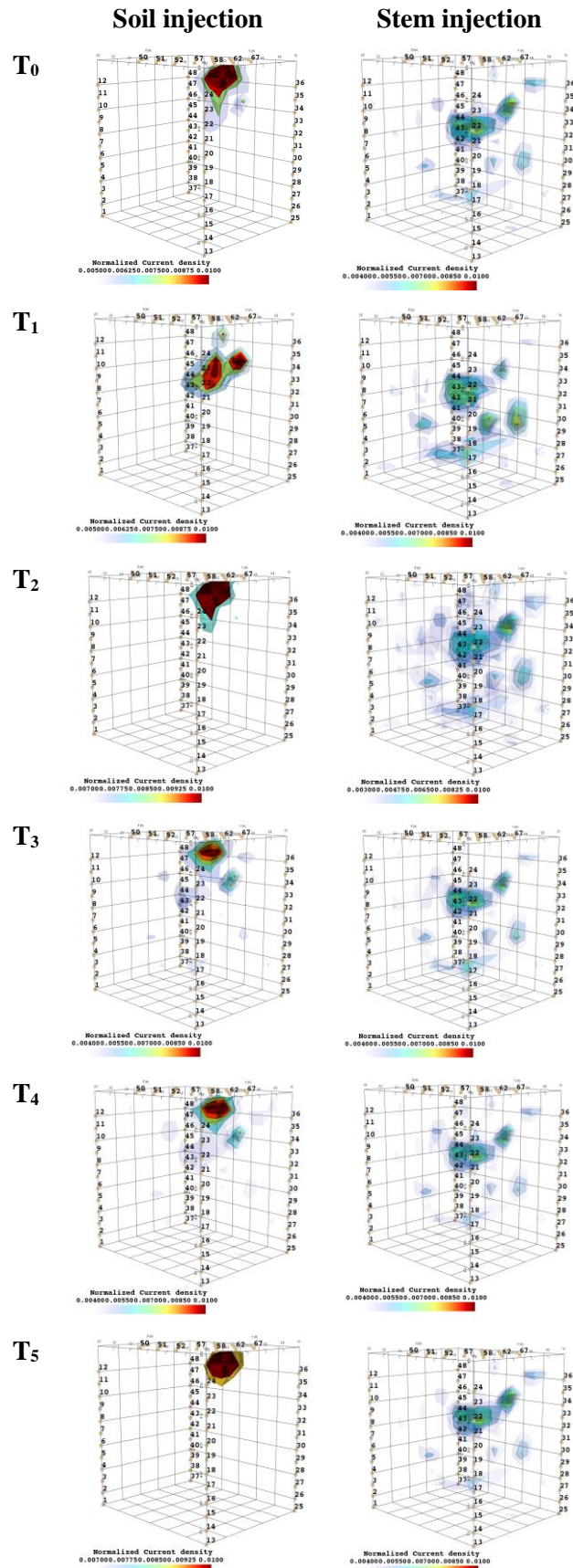
707 Fig. C3: iso-surface minimizing the F1 function for plant A; during stem injection (a), during soil injection (b); Columns
708 represent the six times steps from T0 to T5. Green dot shows plant stem position. Threshold is defined by the misfit 25% of
709 the normalised F1 (value selected according to the evolution of the curve of sorted misfit F1 and calculated for the tree injection
710 at T0 and kept constant for all the time steps).

711
712
713



714
715

716 Fig. C4: Time-lapse evolution of the current source density after minimization of the objective function F2 as defined in Eq.
 717 (3). The results are relevant to the background time T0 to T5 for the plant B, for the soil current injection on the left, and stem
 718 current injection on the right.
 719



720